Multi-Scale Computational Biomechanics of Arterial Diseases

Takami Yamaguchi

Professor
Department of Bioengineering and Robotics, Graduate School of Engineering
E-mail: takami@pfsl.mech.tohoku.ac.jp

Abstract

I have been investigating the cardiovascular system over micro to macro levels by using conjugated computational mechanics analyzing fluid, solid and bio-chemical interactions. In the present study, I introduce our recent researches on the mass transport to saccular aneurysm, cerebral aneurysm growth based on a hemodynamic hypothesis, malaria-infected red blood cell mechanics using a particle method and primary thrombus formation.

1. Introduction

Human cardiovascular system is always under the integrated nervous and humoral control of the whole body, i.e., in homeostasis. Multiple feedback mechanisms with mutual interactions among systems, organs, and even tissues provide integrated control of the entire body. These control mechanisms have different spatial coverages, from the micro- to macroscale, and different time constants, from nanoseconds to decades. I think that these variation in spatial as well as temporal scales should be taken into account in discussing phenomena in the cardiovascular system.

In this background, we have been investigating the cardiovascular system over micro to macro levels by using conjugated computational mechanics analyzing fluid, solid and bio-chemical mechanics. In the present study, I introduce our recent researches on the mass transport to saccular aneurysm, cerebral aneurysm growth based on a hemodynamic hypothesis, malaria-infected red blood cell mechanics using a particle method and primary thrombus formation.

2. Mass Transport to Saccular Aneurysm

Mass transport of biochemical species, such as LDL, oxygen, and ATP, to arterial walls has been postulated to link to atherogenesis [1]. Atherosclerotic wall thickening may have a critical role in the development and rupture of aneurysms. In this section, I present a numerical study on mass transport to walls of saccular cerebral aneurysms at a variety of arterial bends.

2.1. Materials and methods

Computational models are illustrated in Fig. 1. In human cerebral arteries, the Reynolds number and the Womersley number are approximately 200 and 2.0, respectively. Effects of pulsatile flow can be neglected, and we thus calculate steady-state solutions. We solve advection-diffusion equation for mass transport, coupled with Navier-Stokes equation for blood flow field, where the Peclet number is 3.0×10^5 and the Reynolds number is 200. The given wall boundary condition for the mass transport is

$$\frac{\partial c}{\partial n} = Kc, \qquad (1)$$

where the notation c refers to the mass concentration, **n** is the normal vector to the wall, and $K = 5.0 \times 10^{-1}$ is the constant. The Peclet number and the constant represent ATP transport. We use commercial finite volume software FLUENT (Fluent Inc., Lebanon, NH, USA).

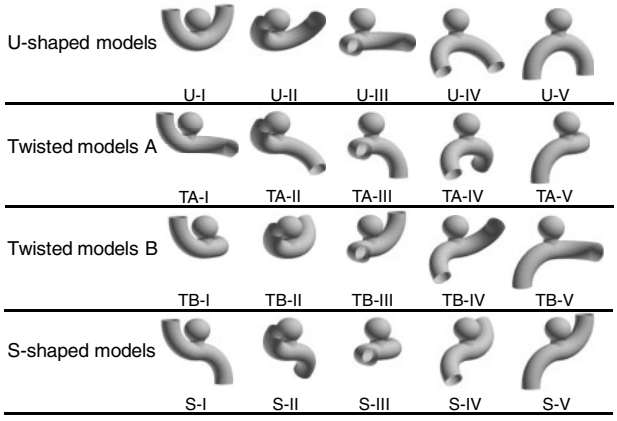

Fig. 1. Computational models

2.2. Results and discussion

Differences of arterial geometry result in a variety of mass concentration profile at aneurysm walls. The averaged concentration is dominated by the inflow flux through the aneurysm neck as shown in Fig. 2. Since the inflow flux is determined by the secondary flow in the parent artery [2], the arterial geometry strongly affects the resultant concentration at the aneurysm walls. The secondary flow also influences on the inflow and outflow pattern, thus vortex structure in the

aneurysm. The minimum concentration is predicted at the center of the vortex near the aneurysm walls as shown in Fig. 3.

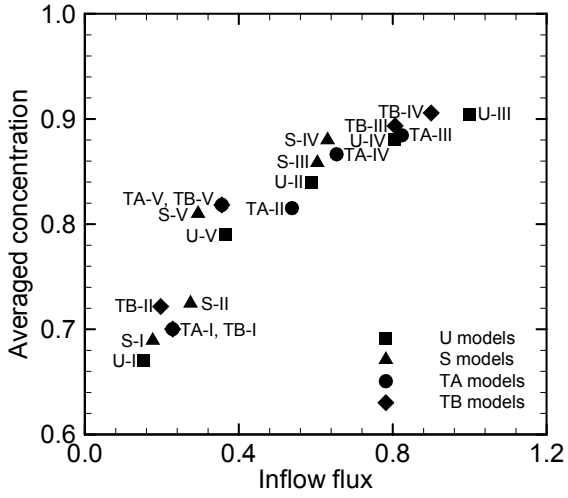

Fig. 2. Relationship between averaged concentration at aneurysm wall and inflow flux into aneurysm

(a)

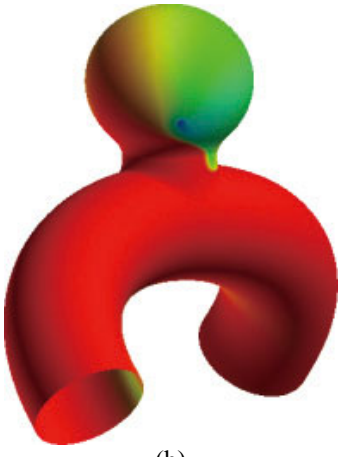

(b)

Fig. 3. (a) Limiting streamline, and (b) concentration at the wall for the model TA-IV

To our knowledge, numerical analysis of mass transport to aneurysm walls has not been conducted previously. Kataoka et al. [3] reported that the inner surface and wall of ruptured aneurysms differ from those of unruptured aneurysms. Our future direction is to reveal the relationship between the mass concentration and the rupture of aneurysms.

3. Cerebral Aneurysm Growth Based on a Hemodynamic Hypothesis

Cerebral aneurysm is an extremely important disease on the clinical medicine, since the rupture of aneurysms causes serious pathologic conditions such as the subarachnoid hemorrhage. The mechanism of aneurysm growth has not yet been understood.

Cerebral aneurysm is characterized by a saccular expansion of the arterial wall. It has been known that strength degradation of the arterial wall is not enough to explain the saccular expansion [4,5]. To understand the phenomena, it should be important to consider biological reactions of the arterial wall. We have focused on increase in the volume of extracellular matrix or in the number of cells in the arterial wall [6], as a candidate for main factor of cerebral aneurysm growth.

It is generally accepted that wall shear stress (WSS) due to blood flow plays an important role in the pathophysiology of aneurysms [7-9]. Moreover, applying high WSS for a long period results in a significant cell proliferation in the arterial wall [6]. We hypothesize, therefore, the biological reactions, such as increase in the number of cells or in the volume of extracellular matrix in the arterial wall, occur locally at the site where WSS is over a threshold value, and the reactions lead to surface area expansion of the arterial wall keeping constant wall thickness.

In this study, we propose a simulation model for cerebral aneurysm growth based on the hypothesis, and perform growth simulations for a cerebral artery model. The computational results are compared with those assuming strength degradation of the wall.

3.1. Modeling and methods

Geometry of the Artery Model

Recently, a lot of researches on a cerebral aneurysm employ arterial geometry based on clinical image data. Such studies are informative and give us detailed information on flow field specific to the patient. In discussing the mechanism of aneurysm formation, however, patient specific analysis gives us the information that is valid only for the patient. It is proposed that cerebral aneurysm may be formed by several different reasons, such as hemodynamic stress, hypertension, or heredity. Thus, the patient specific analysis may lead us to a mechanism suitable specific to the patient. We think it is more appropriate to employ a simple geometric model in order to discuss

general hypothesis and to get basic properties on how aneurysm grow based on the hypothesis.

In this paper, we investigate how an aneurysm is formed in a model cerebral artery with curvature. Figure 4 shows the initial geometry of the artery employed in this study, which is modeled on a part of internal carotid artery. The artery model has 30 mm length along central axis, diameter of 3 mm, curvature radius of 3.6 mm, and torsion of 15°. These values are not much different from former clinical observations.

(a) Front view

(b) Side view

Fig. 4. Geometry of the Artery Model

Blood Flow Simulation

For the calculation of blood flow, it was assumed that blood was an incompressible and Newtonian fluid with a density ρ = 1.05×10^{3} kg/m^3 and the viscosity μ = 3.5×10^{-3} Pa·s. Governing equations for such a blood flow are the equation of continuity,

$$\nabla \cdot \mathbf{u} = 0, \tag{2}$$

and the Navier-Stokes equations,

$$\frac{\partial \mathbf{u}}{\partial t} = -(\mathbf{u} \cdot \nabla)\mathbf{u} - \nabla p + \frac{1}{\mathrm{Re}} \nabla^2 \mathbf{u}, \tag{3}$$

where $\mathbf{u}$ is the three-dimensional velocity vector and p is the pressure. A parameter Re is the Reynolds number defined as $\mathrm{Re} \equiv \rho D u_{\mathrm{ave}} / \mu$, where D is the diameter of the artery and u_{ave} is the averaged velocity at the inlet boundary. In the internal carotid artery, we can assume the quasi-steady blood flow since the Womersley number is about 2-3. Thus, we solved the steady flow at the averaged Reynolds number in the internal carotid artery (Re=200). The change in the diameter of typical cerebral arteries during one pulsation is small and its effect on WSS is not very significant. Moreover, we solve steady flow in this study, so we neglected the wall deformation due to pulsation. Boundary conditions were a parabolic velocity profile at the inlet, zero pressure at the outlet, and the no-slip condition on the wall. Blood flow calculation was accomplished through an in-house three-dimensional flow solver based on MAC algorithm. The total number of grid points was 52,065 (Fig. 5). The accuracy of our numerical code was checked by three-dimensional circular tube flow simulation. And the grid convergence was confirmed by comparing with 103,329 and 205,857 grid points.

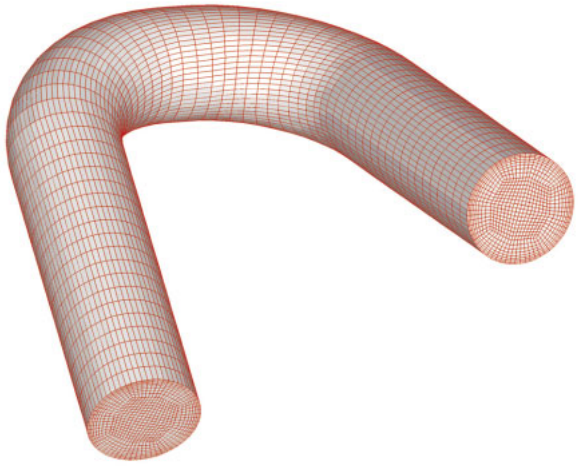

Fig. 5. Computational Grid for Blood Flow

Modeling of Arterial Wall and Its Growth

The arterial wall was discretized by triangle elements. The computational grid generated on the arterial wall is shown in Fig. 5, where 16384 triangle elements (8256 nodal points) were generated. The spring network model [10] was used to mechanically model the arterial wall. In this model, mechanical behavior of the arterial wall was expressed with two types of spring, stretch/compression and bending, as shown in Fig. 6. The stretch/compression spring, which corresponded to a side of a triangle element, expressed the resistance to stretch/compression of the membrane. The other spring expressed the bending resistance of the membrane. Thus, the effect of wall thickness is approximated by this spring. The reason why we used such a simple discretization method is that the accuracy of the wall deformation is strongly limited by the growth model, which will be explained later by eq. (4). We think, therefore, the spring model is good enough to discuss aneurysm growth as a first step.

The arterial wall expansion in the hypothesis may be expressed by nature length elongation of a stretch/compression spring. In this study, we formulated the degree of the elongation as follows.

$$\frac{l_i - l_i^0}{l_i^0} = \alpha(\tau_i - \tau_{th}) \quad \text{if } \tau_i > \tau_{th}, \tag{4}$$

where l_i^0 and l_i are the nature length of the stretch/compression spring element i before and after biological reactions, respectively. τ_i is WSS due to blood flow on the element i and τ_{th} is threshold for WSS. α is a parameter for the degree of the biological reactions. This equation is applied only to the stretch/compression element on which $\tau_i > \tau_{th}$. We employ such a simple linear equation. Since the detail of the relation is still unclear, it is worthwhile starting from a simple model as a first step.

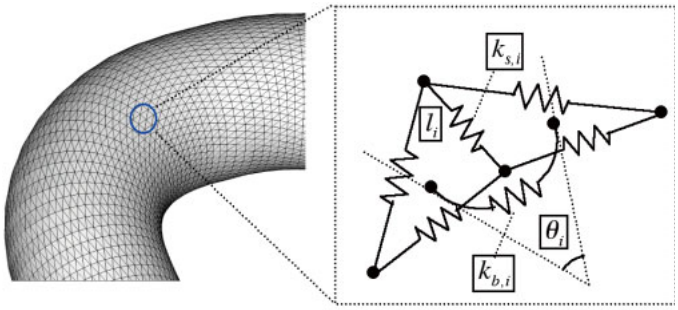

Fig. 6. Mechanical Modeling of Arterial Wall

Wall Deformation Simulation

To solve the deformation of arterial wall due to the change in nature length of springs, we perform the following process; (a) initially change natural length of springs without any deformation, i.e. in the same geometry with Fig. 4, (b) calculate forces acting on each node, (c) move each node during small time step, (d) continue (b) and (c) until convergence criteria is satisfied.

The nature length elongation of a stretch/compression spring without any deformation results in out of balance between the blood pressure force and the internal force of the wall. It is needed to calculate these forces, to simulate the formation of a new equilibrium shape of the artery. We assumed the uniform transmural blood pressure difference of 100 mmHg. The blood pressure force acting on a triangle element was divided equally among three nodes of the element and we express the pressure force acting on node j as $\mathbf{F}_{p,j}$. In this study, spring forces was calculated on the basis of the principle of virtual work [10]. We considered two types of arterial elastic energy, stretch/compression and bending, and then the spring force acting on node j was expressed as follows.

$$\mathbf{F}_{s,j} = -\frac{\partial(E_s + E_b)}{\partial \mathbf{r}_j}, \tag{5}$$

where E_s and E_b are the stretch/compression elastic energy and the bending elastic energy stored in the arterial wall, respectively. $\mathbf{r}_j$ is the position vector of node j. In this study, the calculation of the right-hand side of eq. (5) was accomplished numerically.

The stretch/compression elastic energy E_s was expressed as

$$E_s = \frac{D^2}{2}\sum_{i=1}^{N} k_{s,i}\left(\frac{L_i - l_i}{l_i}\right), \tag{6}$$

where D was characteristic length, which is equal to the diameter in Fig. 1, i is a stretch/compression spring element number, and N is the total number of the elements. $k_{s,i}$ is stretch/compression spring constant, L_i is the present length of the element, and l_i is the nature length given by eq. (6).

In this study, we defined the bending elastic energy E_b as

$$E_b = \sum_{i=1}^{N} k_{b,i} tan^2\left(\frac{\theta_i}{2}\right), \tag{7}$$

where $k_{b,i}$ is bending spring constant of element i, and θ_i, which is shown in Fig. 6, is the bending angle between two neighboring triangle elements. In this equation, we have used tangent function to avoid the folding of the triangle elements [10].

The resultant nodal movement is governed by a set of motion equations for each node,

$$\kappa\frac{\mathrm{d}\mathbf{r}_j}{\mathrm{d}t} = \mathbf{F}_{s,j} + \mathbf{F}_{p,j}, \tag{8}$$

where κ is virtual drag coefficient to control velocity of nodes. The new equilibrium shape of the artery can be obtained by solving the steady solution to eq. (8), since the steady solution satisfies the equilibrium condition;

$$\mathbf{F}_{s,j} + \mathbf{F}_{p,j} = \mathbf{0}. \tag{9}$$

Estimation of Spring Constants

We estimated the bending spring constant so that the bending elastic energy given by eq. (7) was consistent with that given by the shell theory. It was assumed that the arterial wall was an incompressible isotropic elastic media with Young's modulus of 2 MPa, Poisson ration of 0.5, and wall thickness of 0.2 mm. As a result, the bending spring constant was estimated at $k_{b,i}$=1.0×10^{-5} N/m.

One way to estimate the stretch/compression spring constant was to calculate the variation in the arterial diameter when the artery was loaded with transmural pressure, and to compare that with experimental results. We adjusted the stretch/compression spring constant by trial-and-error method so that the arterial diameter

variation calculated in the transmural pressure range 80-120 mmHg was approximately consistent with the experimental result for human internal carotid artery, i.e. stiffness parameter of 11.15 [11]. In this calculation, we used the diameter of 3 mm, which was equal to that in Fig. 1, and the bending spring constant $k_{b,i}$=1.0×10^{-5} N·m as described above. Eventually, the stretch/compression constant was estimated at $k_{s,i}$=1.0 N/m.

When the nature length of a stretch spring becomes n times longer than the initial geometry, the stretch spring constant is reduced to $1/n$ in order to generate equivalent spring forces per strain of the spring, i.e. $\Delta L_i / L_i$, between before and after the growth.

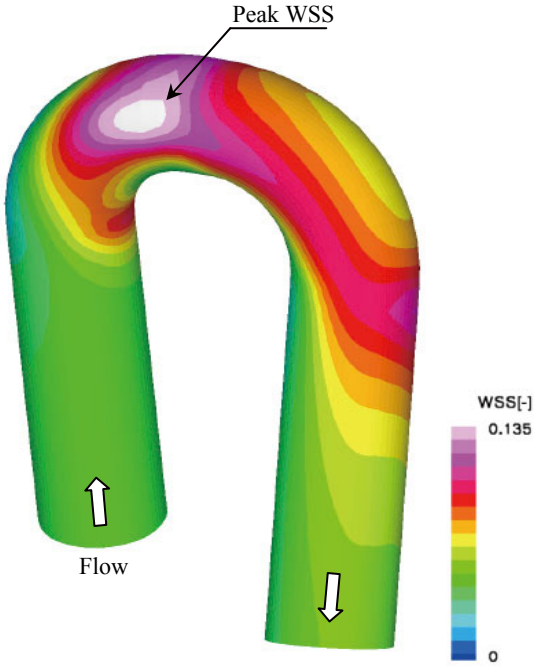

Fig. 7. WSS distribution.

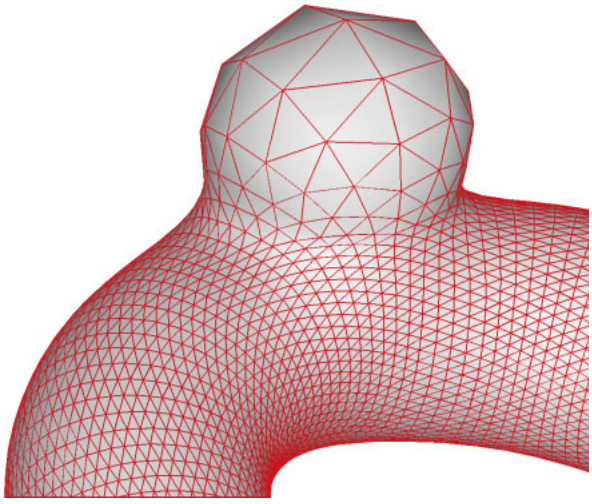

Fig. 8. Result of growth simulation.

All basic equations were non-dimensionarized by the characteristic length D, the averaged velocity u_{ave} at the inlet boundary, the blood density ρ, and the blood viscosity μ.

3.2. Results and discussion

Firstly, we performed the calculation of the steady state blood flow of *Re*=200 for a U-shaped artery with torsion of 15°. Figure 7 shows the distribution of WSS due to blood flow. WSS value was relatively high on the curve and especially high WSS region concentrated on one side of the artery due to the torsion.

Next, we applied the present model to the WSS distribution. The threshold value τ_{th}* was set to 0.12, which was equivalent to 90% of WSS maximum value. Figure 8 shows the result of the growth simulation of a cerebral aneurysm in the case of α=60. Note that the coupling of WSS and shape change was one-way. The resultant shape was consistent with former clinical observations, which indicates the validity of the present model.

We have proposed a simulation model for cerebral aneurysm growth considering the biological reaction and applied the model to a U-shaped artery with torsion. The resultant shape has been consistent with former clinical observations. It is concluded that it is necessary to consider the biological reaction to understand cerebral aneurysm growth and the present model is a powerful tool for understanding the phenomena.

4. Malaria-infected Red Blood Cell Mechanics using a Particle Method

Malaria is one of the most severe infectious diseases all over the world. It causes death of many people in the developing countries of the tropical area. Malaria arises from transmission of plasmodium into blood by Anopheles mosquito. The plasmodium invades red blood cells (RBC). When maturation of the parasite within a RBC, the infected red blood cells (IRBCs) become spherocytic, lose their deformability and develop cytoadherence and rosetting properties. These changes of RBC properties are thought to cause microvascular obstruction, resulting in severe symptoms.

In vitro studies have been performed to investigate mechanical properties of IRBC. The deformability of IRBC was evaluated using optical tweezers [12]. The stiffness of the IRBC was found to increase as the disease progressed. Shelby et al. [13] observed the rheological behavior of single IRBC through micrometer-scale channels that mimicked the capillaries in human body. IRBC at late-stage caused blockages in narrow channels. Cooke et al. [14] identified some ligand-receptor pairs for the cytoadherent property of IRBC. They also reported that most receptor interactions do not show stable binding under flow condition. The IRBCs roll on intercellular

adhesion molecule 1, vascular cell adhesion molecule 1 and P-selectin and rolling IRBCs are arrested at the site of CD36. These studies imply that the complex cell-cell interactions of IRBCs with RBCs and endothelial cells result in the microvascular occlusion. Although experimental techniques have been advanced recently, it is still difficult to observe three-dimensional interactions in microvessels. Numerical modeling can be the means of solving this problem. In this paper, we propose a numerical model of the interaction between RBCs, IRBCs, and endothelial cells in flowing blood. To our knowledge, this is the first application of numerical modeling to Malaria-infected blood flow. The proposed model would contribute on the further understandings of pathophysiology of malaria.

4.1. Method

Tsubota et al. [15] developed a numerical method for modeling RBC behavior in flowing plasma. We extend this method to describe blood flow with IRBCs. In this model, the components of the blood are represented by particles as shown in Fig. 9. We assume the blood to be incompressible Newtonian fluid. The motion of each particle is governed by the following continuity equation and Navier-Stokes equation:

$$\frac{\partial \rho}{\partial t} = 0 \tag{10}$$

$$\frac{D\mathbf{u}}{Dt} = -\frac{1}{\rho}\nabla p + \nu \nabla^2 \mathbf{u} + \mathbf{f} \tag{11}$$

where the notation t refers to the time, $\mathbf{u}$ the velocity vector, ρ the density, p the pressure, ν the dynamic viscosity, and $\mathbf{f}$ the external force. The external force term is used for expressing elastic force of the membrane of RBCs and adhesive force of IRBCs. Equations (1) and (2) are solved by using Moving Particle Semi-implicit (MPS) method [16,17].

The membrane of RBCs is expressed by spring networks as shown in Fig. 10. A membrane particle is connected to neighboring membrane particles with stretch/compression springs. A trio of the particles forms a triangle element. As shown in Fig.10, the element e1 is connected to the element e2 with a bending spring. The deformability of RBC can be adjusted by changing the constants of these stretch and bending springs k_s and k_b.

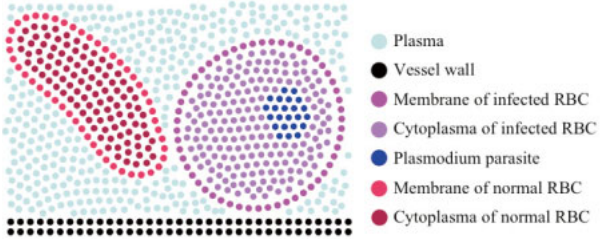

Fig. 9. Particle Model of the Malaria-Infected Blood

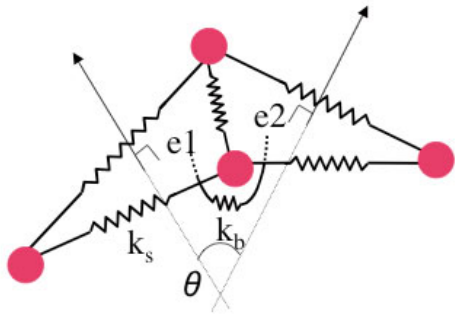

Fig. 10. Spring Model of RBC Membrane

The characteristics of IRBCs are different from those of healthy RBCs. As the plasmodium parasite inside the RBC develops, the shape of the IRBC becomes spherical rather than biconcave. Since the size of the parasite increase, the rigid body of the parasite affects the deformability of the IRBC. In our model, a parasite inside IRBC is expressed by cluster of some particles, which behaves as a rigid object. The developed parasite distorts cytoskeleton and membrane. The membrane of the IRBC becomes stiffer in comparison with healthy RBCs. These changes in the deformability are expressed using large value of the constants of stretch/compression and bending springs. We determined these constants from the comparison between numerical and experimental results of tensile test as shown in the next section.

The adhesive property of IRBC is also modeled by springs. A connection between two particles represents a cluster of many ligand-receptor bindings. If the distance between a particle of IRBC membrane and a particle of endothelial cells or a particle of neighboring RBC membrane is less than a certain value d_{ad}, the two particles are connected by a stretch/compression spring. Figure 11 shows the schematic of the adhesive springs. The spring force between particles i and j is described as

$$\mathbf{f}_{ad} = \kappa\left(1 - \frac{r_0}{|\mathbf{r}_{ij}|}\right)\mathbf{r}_{ij}, \ (|\mathbf{r}_{ij}| \le d_{ad}) \tag{12}$$

where $\mathbf{r}_{ij} = \mathbf{r}_j - \mathbf{r}_i$ is the distance of two particles, r_0 is reference distance, κ is spring constant. Note that once an IRBC membrane particle is connected to a particle of a healthy RBC membrane, the IRBC membrane particle does not connect to the other particle, even if the other particle approaches the IRBC membrane particle within d_{ad}. Maturation of parasites develops knobs on the surface of the membrane of IRBC that mediate cell-cell interaction. That means the increase of the adhesive force. The increase of the adhesive force based on the development of knobs is modeled by increasing the spring constant. In this paper, the spring constant was determined from the experimental results [18].

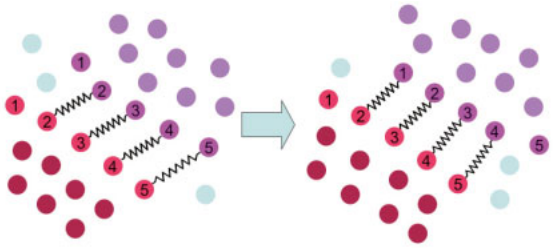

Fig. 11. Adhesion Model by Stretch/Compression Spring

4.2. Results and discussion

We apply the proposed model to flow in the two-dimensional parallel plates with the distance 12 μm. The plasmodium in the IRBC is neglected because the distance is larger than the size of the IRBC. First, we carry out a tensile test to determine the spring constants of membrane. In this test, a RBC and an IRBC is stretched diametrically at force of 151 [pN]. The numerical results are compared with the experimental results in [12]. Since the spring constants $k_s = 3.0 \times 10^{-8}$ [N・m] and $k_b = 5.0 \times 10^{-10}$ [N・m] provide the similar shape of the IRBC at schizont stage observed in the experiment, these values are used as the constants for schizont stage. Figure 12 (a) and (b) shows the steady states in this test for the healthy RBC and the IRBC at schizont stage, respectively. The constants for the other stages are also determined using the same procedure.

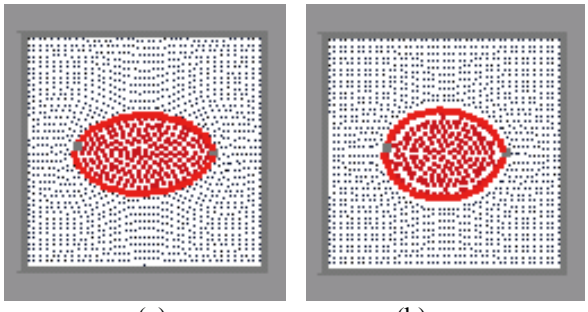

(a) (b)

Fig. 12. Tensile Test
(a) healthy RBC :(b) IRBC at shizont stage

We examine the interaction of a single IRBC with many healthy RBCs. The given boundary conditions are the constant velocity u = 4.0 [mm/s] at the inlet, the constant zero pressure at the outlet, and the no-slip condition at the wall surface. The IRBC is assumed to be at the late-trophozoite stage, where the adhesive coefficient $\kappa = 1.3 \times 10$ [N/m]. Figure 13 shows the snapshots of the numerical results, where the blue particles are adhesive to the other particles. The IRBC moves downstream interacting with endothelial cells and some healthy RBCs. Since the velocity of the IRBC is lower than the other RBCs, a following healthy RBC catches the IRBC. This bonding between the two cells is not so strong that the RBC keeps attachment to the IRBC in short time and eventually detaches from the IRBC.

Figure 14 presents comparison of pressure loss between the flows of plasma, healthy RBCs, a single IRBC and a single IRBC with healthy RBCs. Interestingly, the flow of a single IRBC on the vessel wall causes high pressure loss even without the other RBCs. The result explains that the adhesive interaction between IRBCs and vessel wall plays one of the critical roles on microvascular blockage. The pressure loss of a single IRBC with healthy RBCs flow varies in time because of the complex interaction with the healthy RBCs.

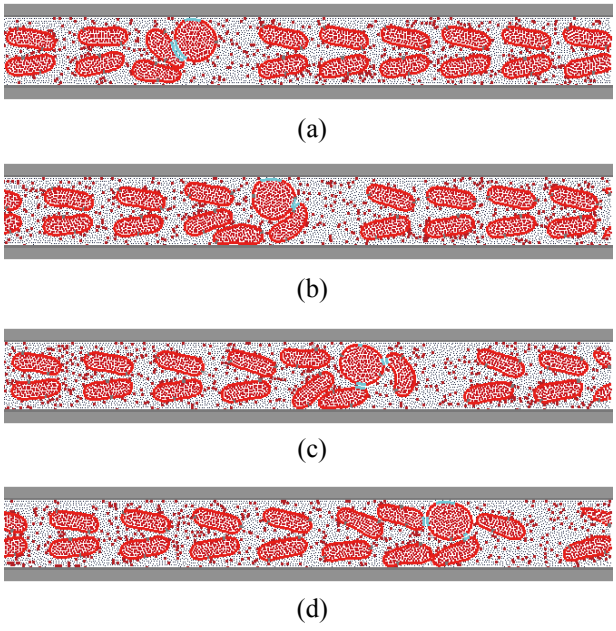

(a)

(b)

(c)

(d)

Fig. 13. Snapshots of the interactions between the IRBC, healthy RBCs and endothelial cells;
(a) t = 4 [ms] :(b) t = 8 [ms]:(c) t = 12 [ms] :(d) t = 16 [ms]

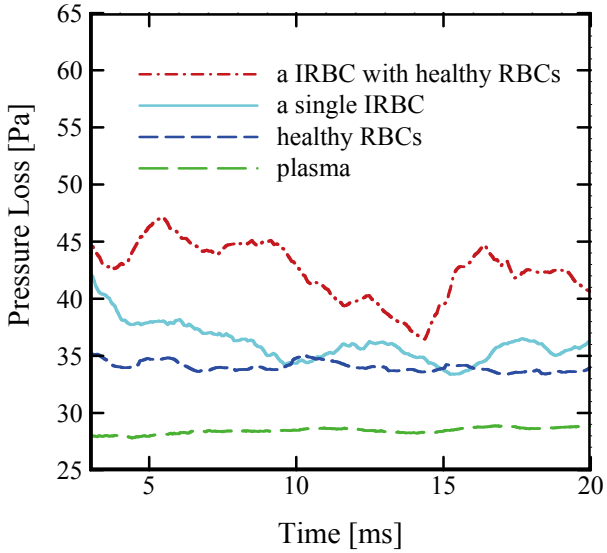

Fig. 14. Pressure loss at various condition

We have developed a numerical model of the blood flow with Malaria-infected RBCs. The interactions between the IRBCs, healthy RBCs, and endothelial cells in flowing blood are expressed by the particle and spring model. In the future study, we improve the proposed model through a variety of comparative studies with the experiments. We hope our model will contribute to the further understandings of pathology of Malaria.

5. Primary Thrombus Formation

It has been pointed out that some mechanical factors play important roles in a series of physiological or biochemical processes during the thrombus formation. Recently, many studies including the authors' work qualitatively demonstrated how the thrombus is regulated under the influences of the blood flow and the intercellular molecular bridge using computational fluid dynamics techniques [19-22]. They verified the importance of the balance of them in the process of the thrombus formation. However, few studies have taken into account the existence of the other cell constituents than the platelet such as red blood cell (RBC).

In the present study, we investigate the influence of the RBCs on the primary thrombus formation under the blood flow using a computational method based on Stokesian dynamics method. We employ Sokesian dynamics method based on the approximation of the additivity of the velocities [23]. The Voigt model is assembled into the method to simulate the binding force due to the intercellular molecular bridge. A monolayer model in which large sized spheres (RBCs) circulate above the layer with small sized spheres (platelets) under a Couette flow is analyzed. The result is compared with the case in which the existence of the RBCs is not considered.

5.1. Methods

Stokesian dynamics method

Our framework follows Stokesian dynamics method which has been developed based on the approximation of the additivity of velocities and applied for ferromagnetic colloidal dispersions by Satoh et al [23]. However, in this study, the binding force mediated by the plasma proteins and the contact force due to direct collision between the platelets or RBCs were introduced instead of the magnetic force. The binding force was modeled using the Voigt model as described in the following section.

We assumed the plasma as incompressible Newtonian fluid, and that the flow field around the cell constituents is governed by the Stokes equation: $\nabla p = \eta \nabla^2 \boldsymbol{u}$, and the equation of continuity: $\nabla \cdot \boldsymbol{u} = 0$, where p is the pressure, η is the viscosity, and $\boldsymbol{u}$ is the velocity vector.

Both the platelet and the RBC were idealized as solid sphere particles. Neglecting Brownian motion, the difference in the density between the cell constituents and the plasma, and the rotational motion of particles, Stokesian dynamics based on the additivity of velocities due to the force exerted on the particle yields the particle velocity of:

$$\boldsymbol{v}_\alpha = \boldsymbol{U}(\boldsymbol{r}_\alpha) + \frac{1}{\eta}\left\{ \boldsymbol{a}'_{\alpha\alpha}\boldsymbol{F}_\alpha + \sum_{\beta=1(\neq\alpha)}^{N} \boldsymbol{a}_{\alpha\beta}\cdot\boldsymbol{F}_\beta \right\} + \sum_{\beta=1(\neq\alpha)}^{N} \tilde{\boldsymbol{g}}_\alpha : \boldsymbol{E}, \quad (13)$$

where $\boldsymbol{U}(\boldsymbol{r}_\alpha)$ is the velocity of background flow filed at the position of particle α, $\boldsymbol{F}_i (i = \alpha, \beta)$ are the forces acting on the particle i, $\boldsymbol{E}$ is the rate-of-strain tensor, $\boldsymbol{a}_{ij}$, $\boldsymbol{a}'_{ij}$, and $\tilde{\boldsymbol{g}}_i$ are the mobility tensors, and N indicates the number of the particles in the system [23]. The mobility tensors can be found in a standard textbook, such as Kim and Karrila [24].

Modeling the binding force due to vWF and Fbg

We assumed that the binding force, $\boldsymbol{F}_i$, results exclusively from two plasma proteins: von Willebrand factor (vWF) and fibrinogen (Fbg), which are known to be main participants in the platelet adhesion and aggregation. Those proteins has been known to have highly distinct properties as follows [25]: (1) Fbg can preferentially bind with GP IIb/IIIa, and the binding is irreversible and efficient with at relatively low wall shear rate (50-500 s^{-1}); (2) In contrast, vWF can bind exclusively with GP Ibα and slightly with GP IIb/IIIa, and the GP Ibα-dependent binding is reversible or transient and more efficient at relatively high wall shear rate rather than at low rate. In order to express such a distinction in the property between Fbg and vWF, we introduced the Voigt model with different character for each protein (Fig. 15 (a), and (b)). Their preferential combination with GP Ibα or GP IIb/IIIa was modeled by setting receptors on each platelet (Fig. 15 (c)).

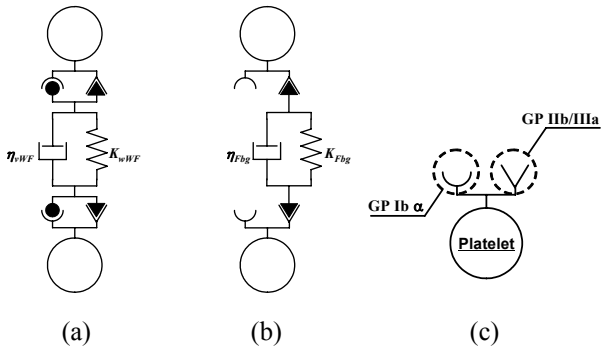

Fig. 15. Voigt models for vWF (a) and Fbg (b), and the receptor models on the platelet (c).

The binding force between two particles i and j was considered when the two particles once come close to each other within a specific distance, $L_0 = 0.5\,[\mu\mathrm{m}]$,

i.e. satisfy $|\boldsymbol{s}| \leq L_0$, where $\boldsymbol{s}$ indicates separation vector expressed as

$$\boldsymbol{s} = \frac{\boldsymbol{r}_j - \boldsymbol{r}_i}{|\boldsymbol{r}_j - \boldsymbol{r}_i|}\{|\boldsymbol{r}_j - \boldsymbol{r}_i| - 2a\}. \quad (14)$$

The Fbg-GP IIb/IIIa association was assumed to be valid when the difference in velocity between two particles is less than a specific value U_{act} = 5.5×10^{-2} [m/s]: $|\boldsymbol{v}_j - \boldsymbol{v}_i| \leq U_{act}$, reproducing the efficiency of Fbg-GP IIb/IIIa association at low shear rate. The vWF-GP Ibα association was assumed to persist only during a specific time T_{act} = 0.5 [s], reproducing the reversibility of vWF-GP Ibα association, Moreover, we assumed that GP IIb/IIIa receptor is activated by vWF-GP Ibα association, and that the associations are broken up when the distance between the two particles exceeds $1.05L_0$. With the above qualifications, the force was expressed as

$$\boldsymbol{F}_{ij}^{(p)} = \frac{\boldsymbol{s}}{|\boldsymbol{s}|}\left[K^{(p)}\{|\boldsymbol{s}| - L_0\} + \eta^{(p)}\frac{|\Delta \boldsymbol{s}|}{\Delta t}\right], \quad (15)$$

where $K^{(b)}$ and $\eta^{(b)}$ are the spring elastic modulus and the dumper viscous coefficient, respectively, and Δt is a time interval. Note that the parenthetic superscript (p) is replaced with (vWF) or (Fbg). Eventually, the binding force acting on a particle i is expressed as

$$\boldsymbol{F}_i^{(b)} = \sum_j \boldsymbol{F}_{ij}^{(vWF)} + \sum_j \boldsymbol{F}_{ij}^{(Fbg)}. \quad (16)$$

We set $K^{(vWF)}$ = 6.0×10^2 [MPa], $\eta^{(vWF)}$ = 3.25×10^{-2} [Pa·s], $K^{(Fbg)}$ = 1.2×10^3 [MPa], $\eta^{(Fbg)}$ = 4.59×10^{-6} [Pa·s], and Δt = 1.0×10^{-9} [s].

Conditions for the simulation

A Couette flow was assumed for the background, and a monolayer model was considered. The luminal surface was constructed by lining particles with 2 [mm] in diameter. RBC particles with 10 [mm] in diameter were inserted between 30±3 [mm] in height from the luminal surface. Platelet particles, which had random size within 2-4 [mm] in radius, were randomly inserted between the luminal surface and the layer of RBCs. A portion of luminal surface was forced to possess ability to bind with platelets via vWF based on the above qualifications to mimic the injured surface.

5.2. Results and discussion

Figures 2 shows some snap shots taken from the results in the case where the existence of RBCs were considered. The aggregate formed onto the injured site gradually grow. However, once the height of the aggregate reaches to the level of circulating RBCs, the aggregate is pushed down due to the RBCs. Comparing the results under the existence of RBCs (Fig. 16) and the absence of them (results not shown) showed that the thrombus covered up the injured site faster in the former case. This suggested that the RBCs may play a role in efficient thrombus formation.

We proposed a numerical method for simulating the process of the primary thrombus formation under the blood flow, the intercellular molecular bridges, and the existence of the RBCs. The effect of the RBCs on the process of the primary thrombus formation was investigated in this study. The results show that the RBCs may play a role in efficient thrombus formation.

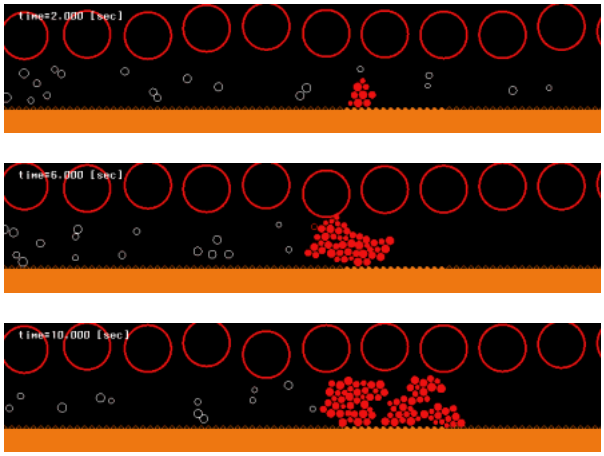

Fig. 16. Simulated thrombus formation under the existence of RBCs at t = 2.0 [s] (upper), t = 6.0 [s] (middle), and t = 10.0 [s] (lower).

Acknowledgements

The author acknowledges support of the Tohoku University Global COE Program, "Nano-Biomedical Engineering Education and Research Network Centre." This research was also supported by "Revolutionary Simulation Software (RSS21)" project supported by next-generation IT program of Ministry of Education, Culture, Sports, Science and Technology (MEXT), Grants in Aid for Scientific Research by the MEXT and JSPS Scientific Research in Priority Areas (768) "Biomechanics at Micro- and Nanoscale Levels", and Scientific Research(S) No. 19100008.

References

[1] Ethier CR. Computational modelling of mass transfer and links to atherosclerosis. *Ann Biomed Eng* **30**, 461-471, 2002.

[2] Imai Y, Sato K, Ishikawa T, and Yamaguchi T. Inflow into saccular cerebral aneurysms at arterial bends. *J Biomech*, 2007 (submitted).

[3] Kataoka K, Taneda M, Asai T, Kinoshita A, Ito M, and Kuroda R. Structural fragility and inflammatory response of ruptured cerebral aneurysms: A comparative study between ruptured and unruptured cerebral aneurysms. *Stroke* **30**, 1396-1401, 1999.

[4] Feng Y, Wada S, Tsubota K, and Yamaguchi T. The application of computer simulation in the genesis and development of intracranial aneurysms. *Technol Health Care* **13**, 281-291, 2005.
[5] Chatziprodromou I, Tricoli A, Poulikakos D, and Ventikos Y. Haemodynamics and wall remodelling of a growing cerebral aneurysm: A computational model. *J Biomech* **40**, 412-426, 2007.
[6] Masuda H, Zhuang Y-J, Singh TM, Kawamura K, Murakami M, Zarins CK, and Glagov S. Adaptive remodeling of internal elastic lamina and endothelial lining during flow-induced arterial enlargement. *Arteioscler Thromb Vasc Biol* **19**, 2298-2307, 1999.
[7] Rossitti S. Shear stress in cerebral arteries carrying saccular aneurysms. A preliminary study. *Acta Radiol* **39**, 711-717, 1998.
[8] Gonzalez CF, Cho YI, Ortega HV, and Moret J. Intracranial aneurysms: flow analysis of their origin and progress. *AJNR Am J Neuroradiol* **13**, 181-188, 1992.
[9] Mori D and Yamaguchi T. Computational fluid dynamics analysis of the blood flow in the thoracic aorta on the development of aneurysm. *J Jpn Coll Angiol* **43**, 94-97, 2003 (in Japanese).
[10] Wada S and Kobayashi R. Numerical simulation of various shape changes of a swollen red blood cell by decrease of its volume. *Trans JSME Ser A* **69**, 14-21, 2003 (in Japanese).
[11] Sato M. *Biomed Eng* **24**, 213-219, 1986 (in Japanese).
[12] Suresh S, Spatz J, Mills JP, Micoulet A, Dao M, Lim CT, Beil M, and Seufferlein T. Connection between single-cell biomechanics and human disease states: gastrointestinal cancer and malaria. *Acta Biomater* **1**, 15-30, 2005.
[13] Shelby JP, White J, Ganesan K, Rathod PK, and Chiu DT. A microfluidic model for single-cell capillary obstruction by plasmodium falciparum-infected erythrocytes. *PNAS* **100**, 14618-14622, 2003.
[14] Cooke BM, Mohandas N, and Coppel RL. Malaria and the red blood cell membrane. *Semin Hematol* **41**, 173-188, 2004.
[15] Tsubota K, Wada S, and Yamaguchi T. Particle method for computer simulation of red blood cell motion in blood flow. *Comput Methods Programs Biomed* **83**, 139-146, 2006.
[16] Koshizuka S and Oka Y. A particle method for incompressible viscous flow with fluid fragmentation. *Nucl Sci Eng* **123**, 421-434, 1996.
[17] Sutera SP and Krogstad DJ. Reduction of the surface-volume ratio: a physical mechanism contributing to the loss of red blood cell deformability in malaria. *Biorheology* **28**, 221-229, 1991.
[18] Chotivanich KT, Dondorp AM, White NJ, Peters K, Vreeken J, Kager PA, and Udomsangpetch R. The resistance to physiological shear stress of the erythrocytic rosettes formed by cells infected with plasmodium falciparum. *Ann Trop Med Parasitol* **94**, 219-226, 2000.
[19] Kamada H, Tsubota K, Wada S, and Yamaguchi T. *Trans JSME Ser B* **72**, 1109-1115, 2006.
[20] Tamagawa M and Matsuo S. *JSME Int J Ser C - Mechanical Systems Machine Elements and Manufacturing* **47**, 1027-1034, 2004.
[21] Wang NT and Fogelson AL. *J Comput Phys* **151**, 649-675, 1999.
[22] Sorensen EN, Burgreen GW, Wagner WR, and Antaki JF. *Ann Biomed Eng* **27**, 436-448, 1999.
[23] Satoh A, Chantrell RW, Coverdale GN, and Kamiyama S. *J Colloid Interface Sci* **203**, 233-248, 1998.
[24] Kim S and Karrila SJ. Microhydrodynamics: Principles and Selected Applications. Butterworth-Heinemann, Stoneham, 1991.
[25] Savage B, Saldivar E, and Ruggeri ZM. *Cell* **84**, 289-297, 1996.